

In-Situ Generation of *N*-Heteroaromatic Polymers: Metal-Free Polymerization and Multiple Functionalities

Yubing Hu,^{†, ‡} Neng Yan,^{||} Xiaolin Liu,^{†, ‡} Lingyu Pei,[†] Canbin Ye,[§] Wen-Xiong Wang,^{||} Jacky W. Y. Lam,^{*, †, ‡} and Ben Zhong Tang^{*, †, ‡, §, δ}

[†]Department of Chemistry, the Hong Kong Branch of Chinese National Engineering Research Center for Tissue Restoration and Reconstruction, Institute for Advanced Study, The Hong Kong University of Science and Technology, Guangdong-Hong Kong-Macro Joint Laboratory of Optoelectronic and Magnetic Functional Materials, Clear Water Bay, Kowloon, Hong Kong 999077, China

[‡]HKUST-Shenzhen Research Institute, No. 9 Yuexing 1st RD, South Area, Hi-tech Park, Nanshan, Shenzhen 518057, China

^{||}School of Energy and Environment, State Key Laboratory of Marine Pollution, City University of Hong Kong, Kowloon, Hong Kong 999077, China

[§]Center for Aggregation-Induced Emission, from Molecular Aggregates, SCUT-HKUST Joint Research Institute, State Key Laboratory of Luminescent Materials and Devices, South China University of Technology, Guangzhou 510640, China

^δAIE institute, Guangzhou Development District, Huangpu, Guangzhou 510530, China

Supporting Information

ABSTRACT: The electron-deficient *N*-heteroaromatic polymers are crucial for the high-tech applications of organic materials, especially in the electronic and optoelectronic fields. Thus, the development of new polymerizations to afford adaptable electron donating-accepting scaffolds in *N*-heteroaromatic polymers is in high demand. Herein, metal-free multicomponent polymerizations of diynes, diamines and glyoxylates are successfully developed for *in-situ* generation of poly(quinoline)s with high molecular weights (M_w up to 16 900) in nearly quantitative yields. By tuning the electron distributions of the polymer backbones, the resulting poly(quinoline)s show various aggregation-induced behaviors and photo-responsive abilities. The thin films of these poly(quinoline)s can be readily fabricated into well-resolved fluorescent photopatterns by photolithography techniques. They can be utilized as fluorescent probes to visualize the morphologies of polymer materials including spherulites and microphase separation of polymer blends. Their nanoparticles demonstrate sensitive and highly selective fluorescence quenching to hexavalent chromium ion Cr(VI), which provides access for the biological imaging of Cr(VI) in unicellular *algae*.

INTRODUCTION

Organic materials are recognized as an important branch of functional materials and have aroused intense academic and technological interest, especially in the electronic and optoelectronic fields.¹ Amongst, polymer materials show superiority than their small molecule counterparts in terms of low-cost, flexibility, high processability and ease for large-scale production.² On the other hand, the development of polymer materials with rational design in their electronic structure³ and intermolecular interactions⁴ is an important topic in polymer science. Generally, the adjustment of electronic structures in polymer materials is achieved by tuning their conjugation length and electron donor-acceptor (D-A) strength.⁵ While high-molecular-weight conjugated polymers suffer from the problems of synthetic difficulty and low solubility⁶, polymers with D-A building blocks display various advantages such as simple synthesis, ease regulation, structure variation and multiple functionalization. To construct D-A scaffold in polymer frameworks, one of the effective strategies is to introduce heteroatoms (e.g., O, N, and S, etc.) to perturb the

electronic distribution along the polymer backbones.⁷ Particularly, the introduction of N atoms in the form of diverse electron-deficient azaromatics is widely applied owing to the high stability, good solubility, diverse intermolecular interactions and unique physicochemical properties of these heterocyclics.⁸ To explore new horizons of *N*-heteroaromatic polymers, the development of concise and adjustable synthetic strategies is needed.

To date, heteroaromatic polymers are mainly constructed by the covalent connection of heteroaromatic monomers through cross-coupling reactions (e.g., Suzuki-Miyaura, Stille, and Heck, etc.) and direct C-H bond activation.^{9,10} These polymerizations are usually catalysed by organometallic reagents or conducted under harsh reaction conditions. Not to mention the cost-consuming reagents and process, the metal residues in the obtained polymers are biological toxic and are harmful to their photophysical properties, which inevitably limit their biological and optoelectronic applications.¹¹ Moreover, the tedious synthesis and narrow monomer scope of the above-mentioned polymerizations greatly confined the type

of polymeric products. On the contrary, natural polymers such as DNA, RNA and protein are composed of various structural units and show considerable structure variations to perform wide biological functions.^{12,13} To mimic the versatility of nature, multicomponent polymerizations (MCPs) stand out as the simplest straightforward methods to achieve structural diversity and multiple functionalities.^{14,15} From the viewpoint of synthetic chemistry, MCPs are derived from multicomponent reactions and thus show many attractive inherited advantages, such as high efficiency, high atom economy and operational simplicity.^{16,17} Although some achievements have been made in this area^{18,19}, the development of metal-free MCPs to construct multifunctional *N*-heteroaromatic polymers from easily available reagents is still charming.

As an important class of *N*-heteroaromatic, quinolines and their derivatives not only serve as structural motifs of alkaloids, but also have found extensive applications in optoelectronics²⁰ and pharmaceuticals and agrochemicals²¹. To embed quinolines in polymer frameworks, different synthetic strategies have been evolved from polycoupling of quinoline monomers²² to *in-situ* formation of poly(quinoline)s through direct polycyclization including Friedländer reaction²³, aza-Diels–Alder reaction^{24,25} and alkyne-aldehyde/aniline reactions²⁶ (Figure 1a). However, the use of metalloid catalysts and the need for harsh reaction conditions in these two-component polymerizations are problems to limit a wide polymer exploration. Therefore, we are motivated to develop metal-free MCPs for the *in-situ* formation of poly(quinoline)s from readily accessible starting materials in a facile and efficient manner. Among MCPs, the A³-coupling of commercially available alkynes, aldehydes and amines has been widely explored as straightforward polymerization methodologies to obtain *N*-containing skeletons,²⁷ including

poly(dipropargylamine)s^{28,29}, poly(tetrahydropyrimidine)s³⁰, poly(dihydropyrrone)s³⁰, and poly(oxazine)s³¹, etc. Furthermore, Bharate et al. reported a formic acid-catalyzed A³-coupling reaction of phenylacetylenes, arylamines and glyoxylates to synthesis quinoline carboxylate esters at room temperature in 2014.³² Based on this reaction, metal-free MCPs of diynes, diamines and glyoxylates have been successfully developed for the facile and efficient synthesis of functionalized poly(quinoline)s under mild reaction conditions (Figure 1b). Since the quinoline ring is electron-deficient, diynes with various electron-donating moieties were then applied to give D–A poly(quinoline)s with different optical properties and aggregation behaviors. Based on the different photo-responsive capabilities, photopatterns can be readily fabricated from their spin-coated polymer films in three kinds of response modes. The incorporation of fluorescent moieties with aggregation-induced emission (AIE) characteristics into the polymer backbones has endowed the resulting poly(quinoline)s with sensitivity to the variation of structural rigidity. Such a property makes them to serve as agents to direct visualize the phase-separation and spherulite morphologies in polymer materials. The AIE-active poly(quinoline)s demonstrated the specific fluorescence response to hexavalent chromium ion Cr(VI) and have been applied for the selective fluorescent detection of Cr(VI) in unicellular *algae*.

RESULTS AND DISCUSSIONS

Polymerization Methodology. To develop this metal-free polymerization for the facile and efficient synthesis of poly(quinoline)s, we used commercially available tetraphenylethene (TPE)-containing diyne (**1a**), 4,4'-oxydianiline (**2a**) and ethyl glyoxylate (**3**) as model monomer

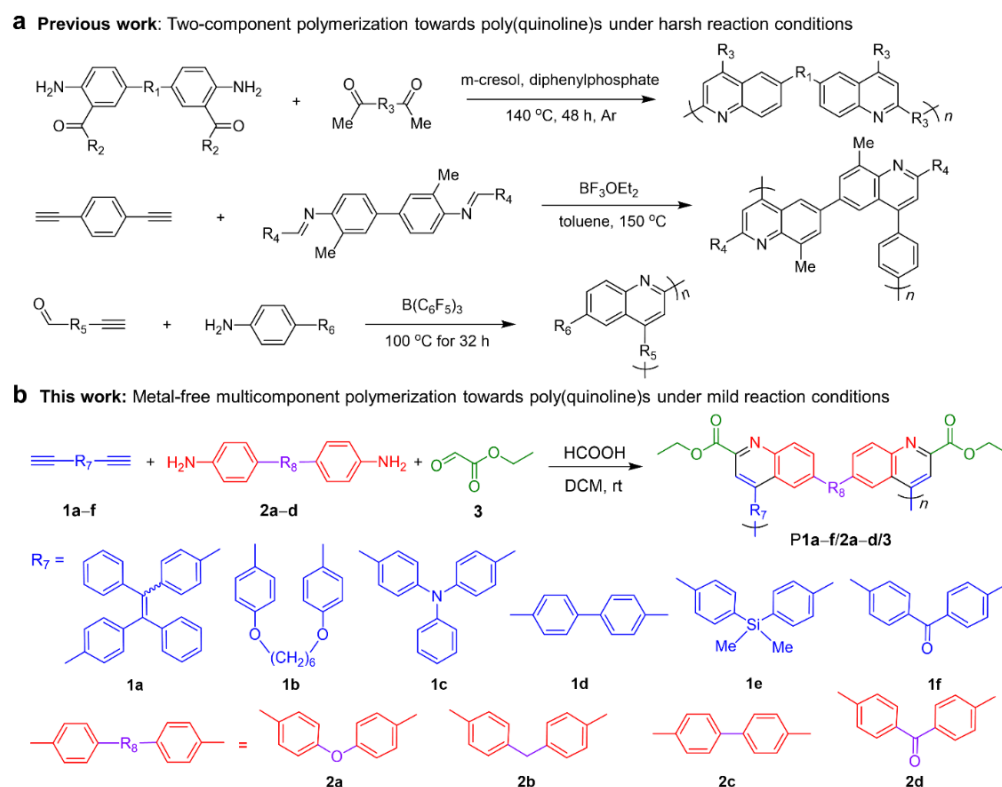


Figure 1. (a) The previous polymerization routes for the *in-situ* formation of poly(quinoline)s. (b) The developed polymerization route towards functionalized poly(quinoline)s **P1a-f/2a-d/3** in this work.

Table 1. Optimization of the polymerization conditions towards poly(quinoline)s^a

no.	solvent	acid (mL)	[3]/[1a]	[1a] (M)	yield (%)	M_w^b	PDI ^b
1 ^c	CH ₃ CN	0.1	2.5	0.2	65.8	9 400	1.96
2	CH ₃ CN	0.1	2.5	0.2	75.4	11 300	1.98
3	DCM	0.1	2.5	0.2	84.0	12 200	1.91
4	THF	0.1	2.5	0.2	26.3	3 700	1.61
5	DMSO	0.1	2.5	0.2	32.8	3 900	1.34
6	DMF	0.1	2.5	0.2	41.2	4 000	1.42
7	DCM	0.2	2.5	0.2	89.6	12 300	1.62
8	DCM	0.3	2.5	0.2	89.3	13 800	1.84
9	DCM	0.4	2.5	0.2	90.6	5 800	1.71
10	DCM	0.3	2.2	0.2	82.8	6 300	1.75
11	DCM	0.3	3.5	0.2	91.7	13 200	1.88
12	DCM	0.3	2.5	0.4	90.6	15 400	2.05
13	DCM	0.3	2.5	0.8	96.7	16 900	1.98

^a Carried out in different solvents and catalyzed by formic acid with various volume under air atmosphere for 3 h at room temperature. [1a] = [2a]. The molar concentration is obtained by dividing the mole of solute by the volume of solvent. ^b Determined by GPC employing THF as eluent on the basis of a linear polystyrene calibration. ^c Carried out in nitrogen atmosphere.

combination to optimize the polymerization conditions. Based on the coupling reaction reported by Bharate et al., the polymerizations were catalyzed by formic acid and carried out at room temperature in a one-pot manner. As listed in Table 1, the effects of various parameters including reaction atmosphere, solvent, catalyst, monomer ratio and concentration were systematically studied to acquire the resulting poly(quinoline)s with high molecular weights in high yields.

The effect of reaction atmosphere was first examined and showed that the polymerization carried out under air behaved better than under nitrogen due to the final oxidation step at the proposed mechanism (entries 1–2). The influence of good solvents for monomers including acetonitrile (CH₃CN), dichloromethane (DCM), tetrahydrofuran (THF), dimethyl sulfoxide (DMSO) and dimethylformamide (DMF) was then investigated (entries 2–6). The best polymerization result was obtained in DCM, which afforded poly(quinoline)s with highest M_w of 12 200 in 84% yield. Next, the volume of formic acid in 1 mL reaction mixture was gradually increased to obtain the most suitable amount of acid catalyst for polymerization. As shown in entries 7–9, the M_w of poly(quinoline)s was finally raised to 13 800 in 89.3% yield. Tuning the molar ratio of [3]/[1a] has a negative effect on the polymerization results (entries 10–11). The monomer concentration was also optimized to obtain soluble poly(quinoline)s with the highest M_w of 16 900 in a nearly quantitative yield (entries 12–13).

Based on the optimized polymerization conditions, the versatility and scope of the polymerizations were investigated and enriched with different combinations of diynes and diamines (Table 2). The terminal diynes **1b–f** were readily synthesized according to the literature methods and the diamines **2b–d** were commercially available. The polymerizations of **1a–f/2a–c/3** proceeded smoothly under mild reaction conditions, generating conjugated poly(quinoline)s with high M_w (up to 16 900) with high yields (up to 97.5%). Such a high efficiency was attributed to the high

Table 2. Polymerizations of different monomers^a

no.	monomer	yield (%)	M_w^b	PDI ^b
1	1a+2a+3	96.7	16 900	1.98
2 ^c	1b+2a+3	93.2	9 800	1.75
3 ^d	1c+2a+3	90.1	12 000	1.94
4	1d+2a+3	83.1	7 200	1.53
5	1e+2a+3	9.6	3 300	1.10
6	1f+2a+3	13.7	2 700	1.13
7	1a+2b+3	95.8	13 900	1.85
8	1a+2c+3	97.5	16 100	2.30
9	1a+2d+3	trace		

^a Carried out in 0.5 mL DCM and 0.3 mL HCOOH for 3 h under air at room temperature. [1] = 0.4 M, [2] = 0.4 M, [3] = 1.2 M, where the concentration of solute is based on the volume of DCM as solvent. ^b Determined by GPC employing THF as eluent on the basis of a linear polystyrene calibration. **P1b/2a/3** and **P1c/2a/3** formed gels under the optimization reaction conditions. ^c Carried out in 0.5 mL DCM for 1 h. ^d Carried out in 1 mL DCM for 3 h.

reactivity of the activated aldehyde groups of glyoxylates. Among these polymers, **P1b/2a/3** and **P1c/2a/3a** under same optimized conditions formed insoluble gels, possibly due to the high reactivity of the flexible and electron-donating monomers **1b** and **1c**. Monomer **1d** with a rigid and short conjugated length gave a polymer with decreased M_w in a moderate yield. The efficiency of polymerizations became lower when silicon-containing and electron-withdrawing monomers (**1e** and **1f**) were used because of their weak nucleophilicity of alkyne groups. The polymerizations of different diamines also produced **P1b/2a/3a** and **P1c/2a/3a** with a high M_w in high yields. However, monomer **2d** failed to be polymerized possibly due to its difficulty to form imine intermediates with glyoxylates. In all, the successful synthesis of **P1a–f/2a–c/3**

demonstrates that this convenient and highly efficient polymerization route provides a great structural diversity of poly(quinoline)s.

The thermal properties of the obtained poly(quinoline)s were evaluated by thermogravimetric analysis (TGA) and differential scanning calorimetry (DSC). TGA results suggest that all the resulting polymers show high thermal stability with 5% weight loss (T_d) at temperatures ranging from 268 °C to 301 °C (Figure S1). The glass transition temperature of the poly(quinoline)s varies from 73 °C to 141 °C due to their different conformational flexibility (Figure S2). All the obtained poly(quinoline)s display good solubility in commonly used organic solvents such as DCM, THF, CH₃CN, DMSO, etc. Their good film-forming abilities are also verified through simple spin-coating process. Their good performance in thermal stability, solubility and processability provides an easy access to explore their multiple functionalities and advanced applications.

Structural Characterization. The FI-IR and NMR spectroscopies have been employed to determine the chemical structures of all the obtained **P1a-f/2a-c/3** accurately. The model compound **M1** was obtained by the formic acid-catalyzed coupling reaction for structural comparison. Taking **P1a/2a/3** for representative structural analysis, its characterization results together with model compound **M1** and the corresponding monomers **1a**, **2a**, and **3** were illustrated in

detail. As shown in the FT-IR spectra of monomers in Figure S3a-c, the stretching vibrations of C≡C and ≡C-H were observed at 2106 and 3275 cm⁻¹, and the stretching and bending vibrations of NH₂ appeared at 3356-3442 and 1620 cm⁻¹. On the other hand, the stretching vibration of C=O and bending vibration of O=C-H were located at 2908-2943 and 1830 cm⁻¹. These functional groups were participated in the A³ reaction and disappeared in the spectra of **M1** and **P1a/2a/3** (Figure S3d and S3e). The formation of C=N in quinolines was associated with the emergence of new vibration peaks at 1714 cm⁻¹ in **M1** and 1685 cm⁻¹ in **P1a/2a/3**. Similarly, all the FI-IR spectra of the obtained poly(quinoline)s displayed no typical absorption peaks associated with the monomer structures and showed C=N stretching vibration at 1661-1689 cm⁻¹ (Figure S4 and S5).

The NMR spectroscopies provided further access to verify the polymer structures. As presented in Figure 2b-f, the acetylene proton of **1a** (H_a), the amino proton of **2a** (H_b) and the aldehyde proton of **3** (H_c) resonated at δ 3.03, 3.50 and 9.42, respectively. All these resonance peaks related to these reactive functional groups were absent in the spectra of **M1** and **P1a/2a/3**, indicating a high extent of the coupling reaction. By comparing with the spectrum of **3**, the proton resonances of the ethyl groups were shifted to low field in the spectra of **M1** (H_d and H_e) and **P1a/2a/3** (H_{d'} and H_{e'}). The formation of quinolines was also confirmed through the analysis of ¹³C NMR spectra in Figure 2g-k. The resonance peaks related to acetylene carbons of **1a** (C_a and C_b) disappeared in the spectra of **M1** and

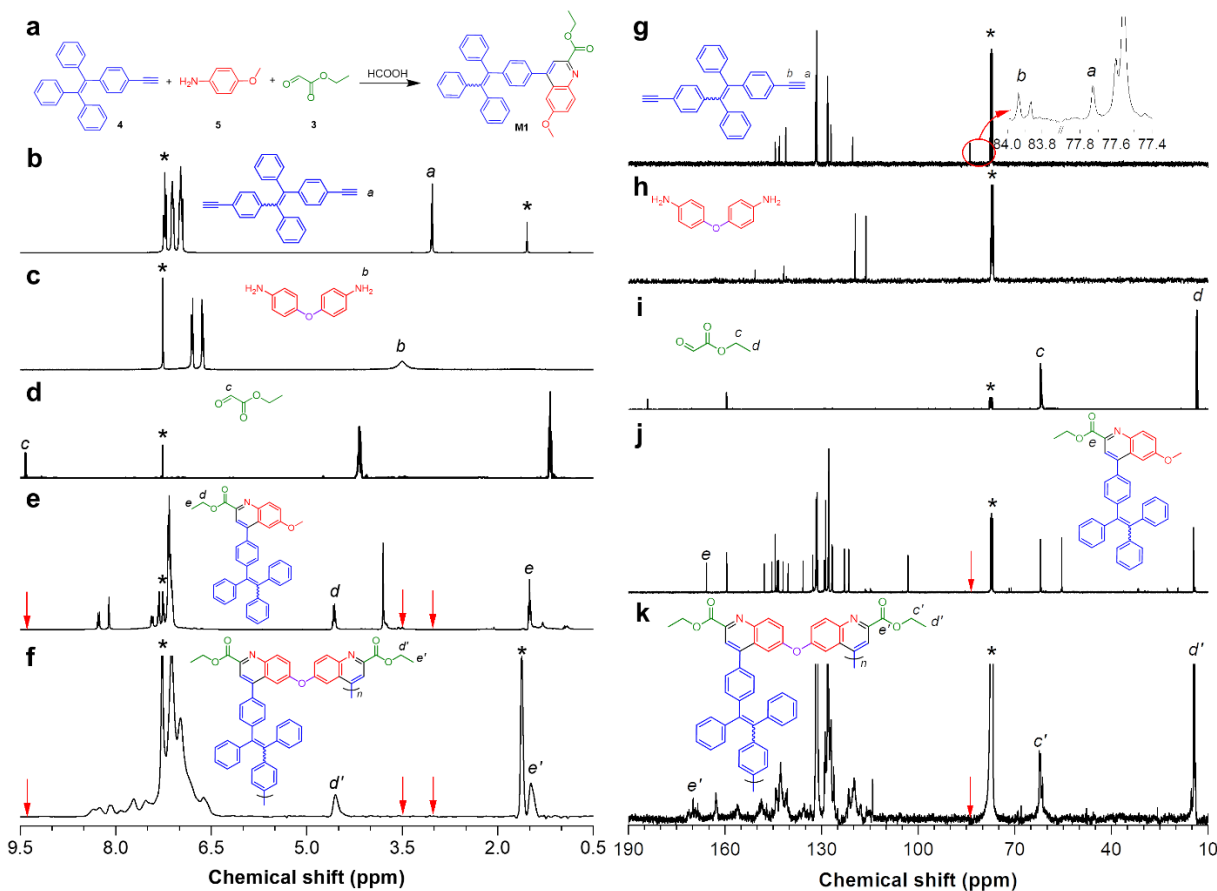


Figure 2. (a) Synthetic route to model compound **M1**. (b-f) ¹H NMR spectra of (b) **1a**, (c) **2b**, (d) **3**, (e) **M1** and (f) **P1a/2a/3** in chloroform-*d*. (g-k) ¹³C NMR spectra of (g) **1a**, (h) **2b**, (i) **3**, (j) **M1** and (k) **P1a/2a/3** in chloroform-*d*. The solvent peaks were marked with asterisks. The resonance peaks related to typical structures of monomers disappeared in the spectra of **M1** and **P1a/2a/3**, as marked by red rows.

P1a/2a/3, revealing the complete consumption of acetylene. The ^{13}C NMR spectra of **M1** and **P1a/2a/3** exhibit the similar carbon resonances of the ethyl groups (C_c and C_d) with the spectrum of **3**. Meanwhile, the resonance peaks at δ 165.69 (C_c) in spectra of **M1** could be assigned to the carbonyl carbon in the quinoline structure, which shifted to δ 169.83 (C_c) in the spectra of **P1a/2a/3**. NMR analysis of **P1a-f/2a-c/3** also confirmed a good correspondence with their chemical structures (Figure S6–S17).

Photophysical Properties. The incorporation of various electron-donating moieties in the conjugated poly(quinoline)s encouraged us to study their photophysical properties. We first investigated the absorption of **M1** and **P1a-f/2a-c/3** in dilute THF solutions (Figure S18). The UV spectra of the polymers exhibited a maximum ranging from 322 to 375 nm. The emission of the polymer powders was screened by simple observation under UV irradiation (Figure S19). By tuning the polymer backbone by using alkyne monomers with different electron-donating abilities, the obtained **P1a-c/2a/3** with TPE, alkoxy-connected phenyl and triphenylamine (TPA) groups were selected for photoluminescence (PL) investigations (Figure 3a–c).

To gain insight into the structure-property relationships, the PL spectra of **P1a-c/2a/3** in THF solutions and THF/water mixtures were systematically investigated (Figure 3d–f). Results showed that the addition of water, the nonsolvent of polymers, lead to an emission improvement for TPE-containing **P1a/2a/3**. Such aggregation-enhanced emission (AEE) phenomenon can be attributed to the restricted molecular motions of TPE moieties in the aggregate state.³³ In fact, TPE is frequently utilized as a AIE-active luminogen to embed the resulting polymers with AIE or AEE characters for multiple applications in the aggregate state.³⁴ While the PL maximum wavelength of **P1a/2a/3** showed no obvious shift, the PL maximum of **P1b/2a/3** and **P1c/2a/3** exhibit varying degrees of bathochromic shift with increasing f_w in THF/water mixtures. With same electron-withdrawing carbonyl-functionalized quinolines, **P1b-1c/2a/3** were introduced with stronger electron-donating groups than **P1a/2a/3**. Hence, the intramolecular charge transfer (ICT) of the donor- π -acceptor structures in **P1b-1c/2a/3** made their emission gradually redshift with increasing polarity in THF/water mixtures. Such redshift variation in **P1b-1c/2a/3** can be also found in the comparison of their solution and solid state in Figure S20 and

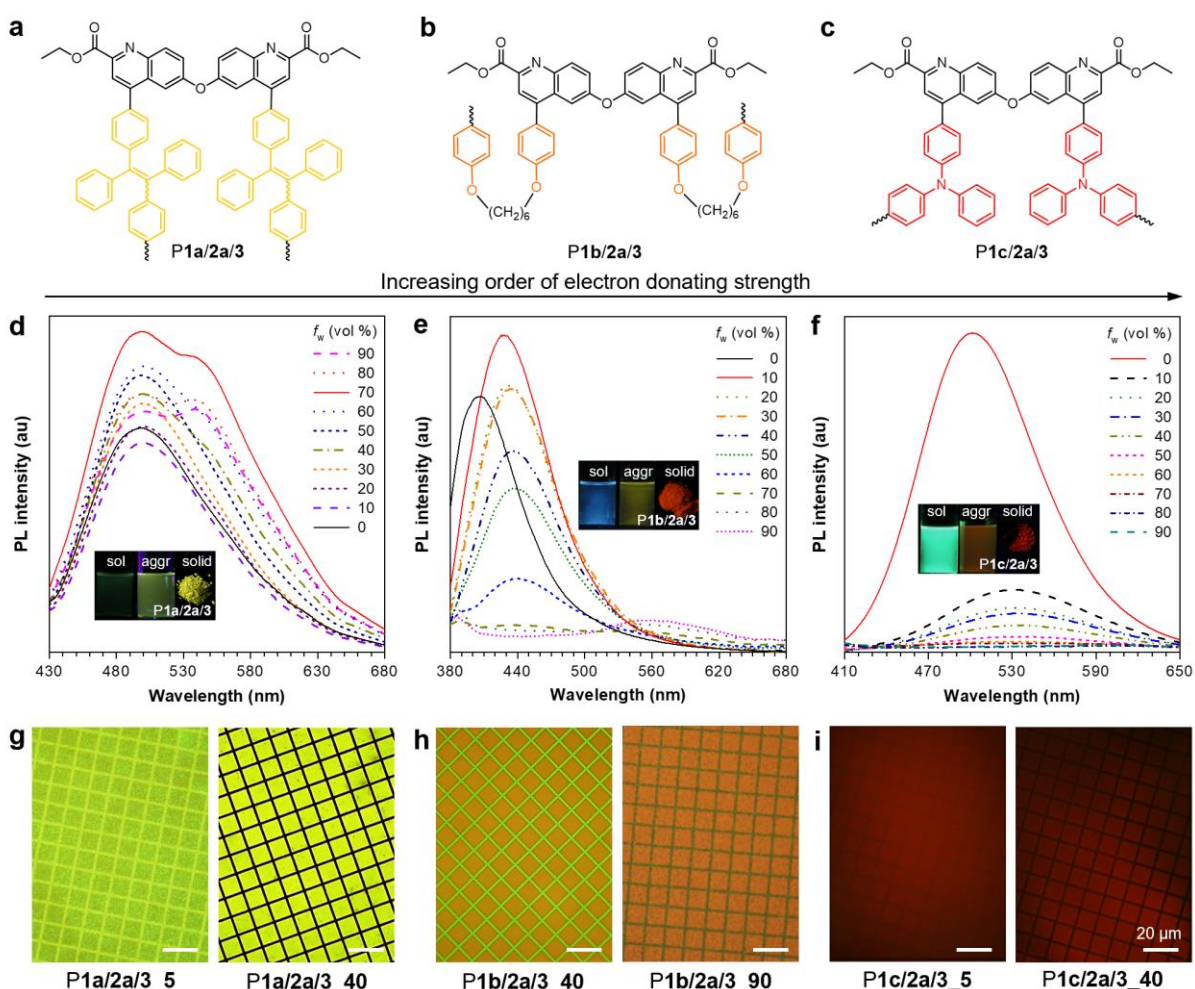


Figure 3. Chemical structures and PL spectra of (a and d) **P1a/2a/3**, (b and e) **P1b/2a/3** and (c and f) **P1c/2a/3** in THF/water mixtures (50 μM) with different water fractions (f_w). Excitation wavelength: 350 nm for (d and e) and 380 nm for (f). Inset: Photos of emissive species in pure THF, THF/water mixture and solid state taken under 365 nm UV light. (g–i) Two-dimensional fluorescent photopatterns generated by the photo-masked UV irradiation of polymer thin films on silicon wafers. (g) **P1a/2a/3** irradiated for 5 and 40 min, (h) **P1b/2a/3** irradiated for 40 and 90 min, and (i) **P1c/2a/3** irradiated for 5 and 40 min.

Table S1. Interestingly, a new shoulder peak at around 540 nm emerged in the PL spectra of **P1a/2a/3** at $f_w > 50\%$. To further understand this phenomenon, the PL spectra of **M1** and TPE-containing **P1a/2b/3** in THF/water mixtures were studied in Figure S21. Obviously, the small molecular **M1** showed a single peak enhancement while **P1a/2b/3** showed a similar red-shifted shoulder peak after adding water. This implies the possible existence of through-space conjugation in the entangled and compact polymer aggregates through multiple inter-/intra-molecular interactions, which induces the intensified and red-shifted emission of **P1a/2a-2b/3** aggregates. Meanwhile, the dual excitation peaks and excitation-dependent emission further supported the presence of through-space conjugation and the additive clusterization-triggered emission peak of **P1a/2a/3** aggregates (Figure S22).³⁵

Based on their good film-forming property and solid-state emission, it is promising to fabricate the poly(quinoline)s into microscale fluorescent photopatterns. The thin films of **P1a-c/2a/3** were prepared by simple spin-coating of their solutions on silicon wafers and then were exposed to UV light for n minutes (**P1a-c/2a/3_n**) through a negative copper photomask. Such photolithography process will usually keep the emission of the copper-protected squares and change the emission of the exposed crosslines based on the photosensitivities of polymer films. As shown in Figure 3g-i, **P1a-c/2a/3** behaved different time-dependent photo-responsive behaviors and displayed three photopatterning modes as on-off, dual-off and weak-off, respectively. Due to the photobleaching of all emitting moieties by sufficient UV irradiation, it is easy to understand that the crosslines of **P1a-c/2a/3** are all quenched in the end and lead to well-resolved negative two-dimensional photopatterns. Moreover, their photo-responsive difference under insufficient UV irradiation attracts our attention for further verification experiments. The GPC curves of **P1a-c/2a/3** solutions in THF after 0 to 100 min of UV irradiation and the corresponding PL spectra of **P1a-c/2a/3** in the aggregate state, as well as the ¹H NMR spectrum of UV-irradiated **M1** were collected in Figure S23-S25. The gradual photodegradation of **P1a-c/2a/3** over time and the evident changes of NMR resonance peaks in the

aromatic and alkyl proton region of **M1** illustrates the photo-induced structural decomposition of quinolines through complicated photo-oxidation reactions. However, the photodegradation of quinolines generated three types of fluorescence response. After a short period of UV irradiation, the poly(quinoline)s aggregates demonstrated enhanced cluster emission for **P1a/2a/3**, intensified blue-shifted emission for **P1b/2a/3** and weaken emission for **P1c/2a/3**, which are consistent with their corresponding photopatterned films. This indicates the involved photochemical process for **P1a-c/2a/3** is reliable and the resulting three types of photoresponsive behaviors can be employed for further technological applications in anti-counterfeiting and optoelectrical devices.^{36,37} Collectively, the present polymerization methodology provides a facile and simple tool to construct poly(quinoline)s with adaptable photophysical properties and photo-sensitivities.

Morphological Visualization. A single polymer material is hard to meet the practical requirements of variety and high performance, and polymer blends thus have been intensively developed, in which two or more polymers are physically mixed. The study of compatibility between polymer components is of great academic and technical importance, which can be evaluated through the morphology of the polymer blends. Therefore, the effective method that can visualize the morphology of polymer blends is in great demand. Recently, our group has achieved high-contrast visualization of microphase separation in polymer blends by fluorescent AIE-active small molecules.³⁸ Since polymer materials possess advantage of structure variation and easy fabrication, the performance of the polymer-based AIE-active probe in such a situation can be explored.

The AEE-active **P1a/2a/3** was taken as a representative fluorescent indicator to observe the mesoscale morphologies of polymer blends. The photos of thin films of homopolymers including polybutadiene (PB), polystyrene (PS), poly(methyl methacrylate) (PMMA) and poly(ethylene glycol) (PEG) with 1 wt% of **P1a/2a/3** were taken under UV light and given in Figure 4a-d. The images of PB, PS and PMMA showed smooth

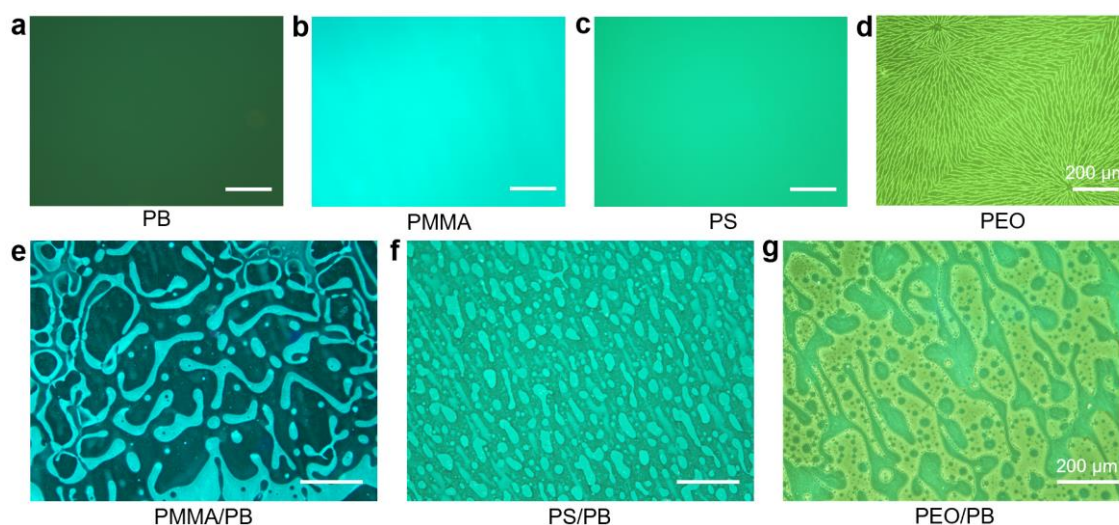


Figure 4. Fluorescent images of polymer films with 1 wt% of **P1a/2a/3** as fluorescent indicators prepared from (a) PB, (b) PMMA, (c) PS, (d) PEO and (e-g) polymer blends of two polymers with a mass ratio of 1:1: (e) PS and PB, (f) PMMA and PB, and (g) PEO and PB.

morphologies with different emission intensity possibly due to their different structural rigidity and through-space conjugation (Figure S26). The heteroatom-rich polymers (PMMA and PEO) tend to interact with poly(quinoline)s via through-space electronic communications like π - π and n - π , leading to strongly enhanced emission.³⁹ Interestingly, a clear spherulitic morphology was observed in the thin film of semicrystalline PEG in the presence of **P1a/2a/3**. The spherical textures radiated from the multiple spherical centers were composed of strongly-emissive crystallites and weakly-emissive amorphous parts, which provides a simple and high-contrast way to identify the fine texture of polymer spherulites.³⁰ To utilize the weak emission of PB homopolymers, the polymer blends of PS-PB, PMMA-PB and PEG-PB with weight ratio of 1:1 were prepared with 1 wt% of **P1a/2a/3** to induce the phase separation.

According to the emission difference of their corresponding homopolymers, it is easy to assign the weak-emissive matrix to the PB phase in Figure 4e-g. The strongly-emissive domains which demonstrated as isolated islands, were the PS and PMMA phases, while the PEG domains still contained the PB phase inside. These distinct phase-separation patterns reflected the partial compatibility of PS, PMMA and PEG with PB. Thus, these results suggest that fluorescence microscope coupled with TPE-containing poly(quinoline)s is a powerful tool to visualize the morphologies of polymer materials in the mesoscale, including the fine texture of spherulites and microphase separation of polymer blends.

Fluorescence Detection of Cr(VI). Hexavalent chromium ion Cr(VI) is highly carcinogenic and mutagenic and can cause allergic reactions, hereditary genetic defects and various types

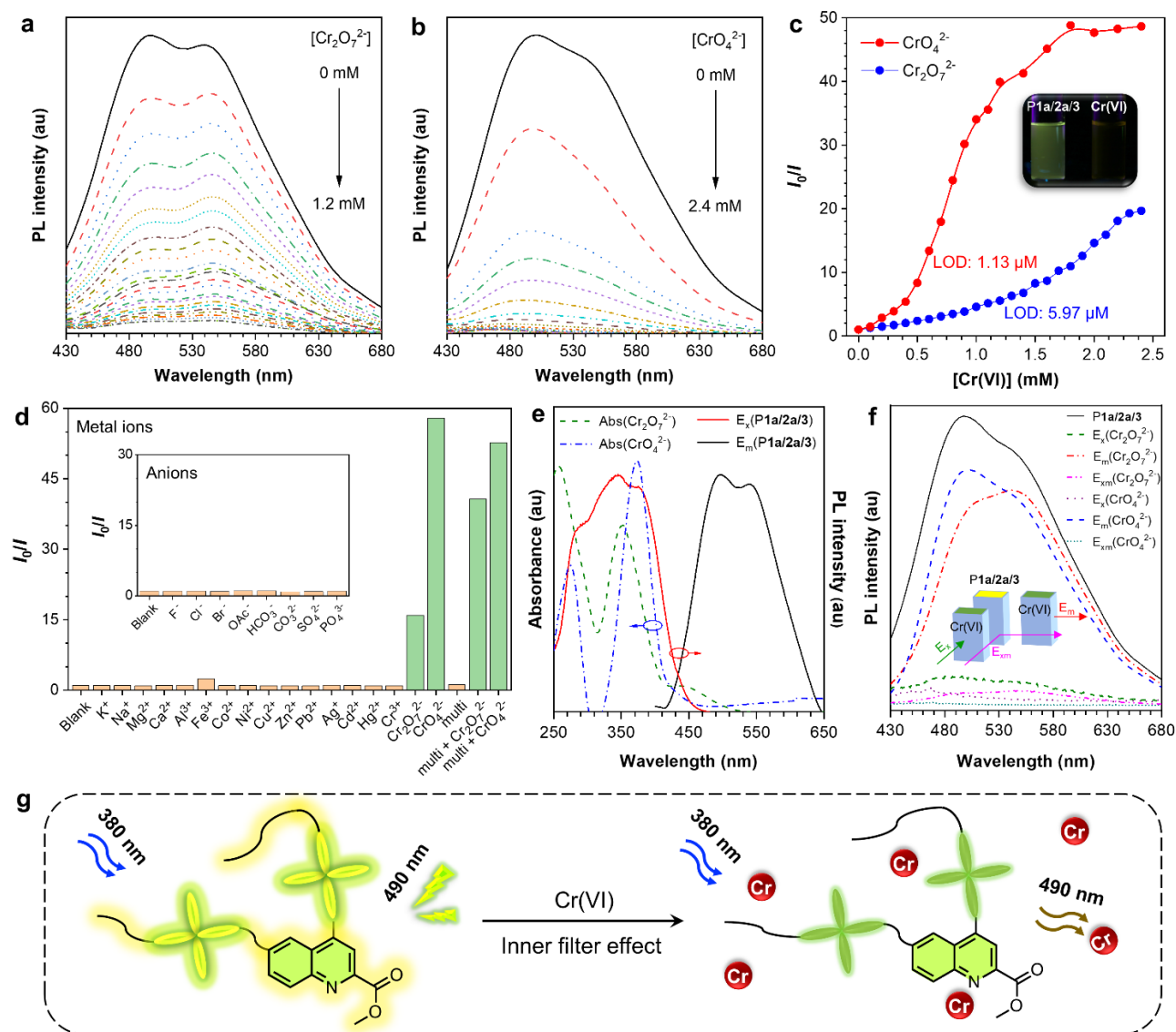


Figure 5. (a and b) PL spectra of **P1a/2a/3** (50 μ M) in THF/water mixture with $f_w = 70$ vol% at different concentrations of (a) $\text{K}_2\text{Cr}_2\text{O}_7$ and (b) K_2CrO_4 . (c) Plot of relative emission intensity (I_0/I) of **P1a/2a/3** versus the concentration of Cr(VI), where I_0 = peak intensity of pure **P1a/2a/3**. Inset: Fluorescent photos of **P1a/2a/3** without or with Cr(VI) taken under 365 nm UV light. (d) Relative emission intensity (I_0/I) of **P1a/2a/3** in the presence of various metal ions and anions (2 mM). (e) Overlapping of the absorption spectra of $\text{K}_2\text{Cr}_2\text{O}_7$ and K_2CrO_4 , and the excitation spectra and emission spectra of **P1a/2a/3**. Excitation wavelength: 380 nm. (f) PL spectra of **P1a/2a/3** (50 μ M) in THF/water mixture with aqueous solutions of $\text{K}_2\text{Cr}_2\text{O}_7$ or K_2CrO_4 placed in the excitation path or emission path. Inset: The simple setup for PL measurements. (g) Proposed mechanism of Cr(VI) detection as the inner filter effect.

of cancers. A facile and versatile strategy for highly selective sensing of Cr(VI) is thus meaningful to public health. To investigate the probably of the resulting emissive poly(quinoline)s as Cr(VI) sensor, the TPE-containing **P1a/2a/3** nanoaggregates in water/THF mixture ($f_w = 70\%$) was selected in the following study. Since the balance of Cr(VI) species between $\text{Cr}_2\text{O}_7^{2-}$ and CrO_4^{2-} is pH-dependent, the pH effect on the emission intensity of **P1a/2a/3** was monitored in various buffer solutions (Figure S27). Only slight intensity change was observed with pH ranging from 1 to 10, which underlined its practical applicability in a wide pH range. The sensitivity measurements of **P1a/2a/3** nanoaggregates to Cr(VI) were conducted by adding $\text{K}_2\text{Cr}_2\text{O}_7$ and K_2CrO_4 with Cr(VI) concentrations changing from 0 to 2.4 mM (Figure 5a and 5b). Results showed the evident decreasing emission intensity upon the addition of both Cr(VI) species. The relative emission intensity ratio (I_0/I) versus Cr(VI) concentration is plotted in Figure 5c, where I_0 = peak intensity without Cr(VI). Results show that the emission quenching effect of CrO_4^{2-} is more profound than $\text{Cr}_2\text{O}_7^{2-}$ and they both arrive the quenching limitation in the studied Cr(VI) concentration range. The relationship between the PL intensity and the Cr(VI) concentration in the initial five points was linearly fitted. Based on 3 times the standard deviation of the blank, the limit of detection of the fluorescent sensor was calculated as $5.97\ \mu\text{M}$ for $\text{Cr}_2\text{O}_7^{2-}$ and $1.13\ \mu\text{M}$ for CrO_4^{2-} . Compared to the limitation value of $1.9\ \mu\text{g/L}$ in drinking water advised by US Environmental Protection Agency, the Cr(VI) fluorescent sensor in basic conditions is acceptable.

To evaluate the selectivity of Cr(VI) detection, the effect of common anions and metal ions on PL emission of **P1a/2a/3** was measured and their quenching ratios (I_0/I) were calculated as given in Figure 5d and Figure S28. Compared to other metal ions (K^+ , Na^+ , Mg^{2+} , Ca^{2+} , Al^{3+} , Fe^{3+} , Co^{2+} , Ni^{2+} , Cu^{2+} , Pb^{2+} , Ag^+ , Cd^{2+} , Hg^{2+} and Cr^{3+}) and various anions (F^- , Cl^- , Br^- , OAc^- , HCO_3^- , CO_3^{2-} , SO_4^{2-} and PO_4^{3-}), the fluorescent sensing of Cr(VI) is more specific with an emission quenching ratio of over 16-fold. In addition, the interference of co-existing ions was also evaluated by using the mixture of all the mentioned anions, which is shown as “multi” column. The presence of

multi-ions has no interference on the determination of CrO_4^{2-} . The enhanced quenching ratio to $\text{Cr}_2\text{O}_7^{2-}$ indicates its transition to CrO_4^{2-} in the presence of basic salts such as OAc^- and HCO_3^- . The **P1a/2a/3** can not only specifically detect Cr(VI) with no interference from ion mixture, but also differentiate the existing species of Cr(VI).

For mechanism study, the fluorescence quenching of chemosensing always involves the interaction with analytes or intermolecular energy transfer. The absorption spectra and dynamic light scattering results were measured upon additions of $\text{Cr}_2\text{O}_7^{2-}$ and CrO_4^{2-} , which demonstrate no evident change of absorption maximum and particle size (Figure S29 and S30). This excludes the possibility for the formation of **P1a/2a/3**-Cr(VI) complex. Then the absorption spectra of $\text{Cr}_2\text{O}_7^{2-}$ and CrO_4^{2-} were compared to the excitation and emission spectra of **P1a/2a/3** in Figure 5e. The large overlapping between the absorption of analytes and the excitation/emission of detector indicates that the possible intermolecular energy transfer results in fluorescent quenching. Such sensing mechanism is called as inner filter effect (IFE). To further verify the hypothesis, we measured the PL spectra of **P1a/2a/3** with aqueous solutions of $\text{Cr}_2\text{O}_7^{2-}$ or CrO_4^{2-} placed in the excitation path or emission path (Figure 5f). Results demonstrate the major contribution from the excitation process and minor contribution from the emission process on the fluorescence quenching. Based on these detailed studies, the TPE-containing poly(quinoline)s nanoparticles are found with sensitive and highly selective fluorescence sensing to Cr(VI) ions.

Biological Imaging of Cr(VI). The good performance of **P1a/2a/3** nanoaggregates in fluorescent sensing of Cr(VI) encourage us to examine their potential applicability in biological Cr(VI) imaging. The biocompatibility of **P1a/2a/3** nanoaggregates was investigated by exposing cells to various concentrations of **P1a/2a/3** for 96 h, which demonstrated the cell viability was not obviously influenced at a polymer concentration ranging from 0 to $50\ \mu\text{M}$ (Figure S31). The freshwater unicellular *algae*, the simplest biological systems, was stained with $50\ \mu\text{M}$ of **P1a/2a/3** nanoaggregates for 4 h. The confocal fluorescent images illustrated that cellular uptake of **P1a/2a/3** was effective after incubated with $50\ \mu\text{M}$ of

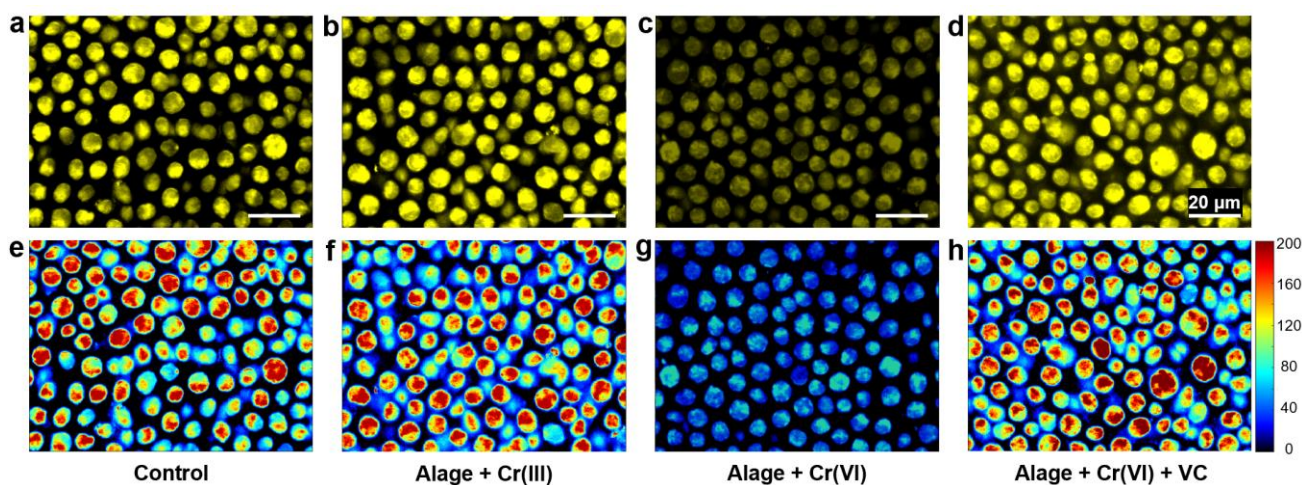


Figure 6. (a–d) Confocal images and (e–h) corresponding heat images of *unicellular algae* incubated with **P1a/2a/3** ($50\ \mu\text{M}$) for 4 h. (a and e) control experiment; (b and f) incubated with Cr(III) (2 mM); (c and g) Cr(VI) (2 mM); (d and h) Cr(VI) (2 mM) and Vitamin C (5 mM). Excitation wavelength: 405 nm. Emission range: 450–650 nm.

P1a/2a/3 for 24 h (Figure 6a and 6e). Unlike the highly toxic and carcinogenic Cr(VI), trivalent chromium (Cr(III)) is an essential element in humans with a recommended daily intake of 50 to 200 $\mu\text{g/d}$. Based on the PL results in Figure 5d, **P1a/2a/3** nanoaggregates provides us a powerful method to differentiate Cr(VI) and Cr(III) in solutions. As shown in Figure 6b and 6f, the co-incubation with Cr(III) had a little effect on the emission intensity of **P1a/2a/3** in *algae*. In contrast, the obvious “on-off” emission in Figure 6c and 6g indicate the evident increment in the intracellular Cr(VI) level after Cr(VI) co-incubation. To perform reduction of Cr(VI) to Cr(III), the vitamin C (ascorbic acid) was selected as the reductant and its performance on fluorescent recovery has been verified by PL tests in Figure S32. Then the *algae* incubated by Cr(VI) was further cultivated with vitamin C for 24 h to transfer intracellular Cr(VI) to Cr(III). Results in Figure 6d and 6h demonstrate the largely restored “off-on” emission intensity of **P1a/2a/3** in *algae* and imply the successful intracellular reduction of Cr(VI) to Cr(III). These results indicate that the resulting poly(quinoline)s realize the “on-off-on” biological Cr(VI) imaging in a simple, high selective, on-site manner.

CONCLUSIONS

In this work, we developed a facile and highly efficient polymerization route for the metal-free synthesis of electron-deficient poly(quinoline)s from readily accessible diynes, diamines and glyoxylates. This versatile polymerization can yield poly(quinoline)s with high molecular weights (M_w up to 16 900) in near quantitative yields. By simply changing the electron-donating moieties in the polymer backbone, the resulting poly(quinoline)s with various D–A strengths are rendered with different aggregation-triggered fluorescence behaviors and tunable emission color from green, orange to red. The good film-forming ability and divergent photo-sensitivity of these poly(quinoline)s enable their thin films to fabricate high-resolution 2D fluorescent photopatterns operated in different modes. Thanks to the restricted molecular motions in rigidified morphologies, the TPE-containing poly(quinoline)s can serve as fluorescent indicators to visualize the phase separation of polymer blends and differentiate the crystallites and amorphous part of polymer spherulites. The nanoparticles of TPE-containing poly(quinoline)s demonstrate to be sensitive and selective fluorescence sensors to highly toxic Cr(VI). The fluorescence quenching of Cr(VI) was proved to be the inner filter effect. Such a non-irradiation energy conversion demonstrate a flexible and straightforward technique for the differentiation of Cr(VI) and Cr(III) in biological system. It is anticipated that this work can broaden the platform of metal-free multicomponent polymerizations and enrich the structure diversity of *N*-heteroaromatic polymers with D–A scaffold to promote the future applications of heteroaromatic polymers in optoelectronics and sensors.

ASSOCIATED CONTENT

Supporting Information

The Supporting Information is available free of charge on the ACS Publications website at <http://pubs.acs.org>. Detailed synthesis procedures, structural characterizations and supporting property investigation can be found in the Supporting Information.

AUTHOR INFORMATION

Corresponding Authors

*chjacky@ust.hk
*tangbenz@ust.hk

ORCID

Yubing Hu: 0000-0003-3083-0067
Neng Yan: 0000-0003-4662-4348
Xiaolin Liu: 0000-0002-6909-117X
Wen-Xiong Wang: 0000-0001-9033-0158
Jacky W. Y. Lam: 0000-0001-5754-1703
Ben Zhong Tang: 0000-0002-0293-964X

Notes

The authors declare the following competing financial interest.

ACKNOWLEDGMENT

This work was financially supported by the National Natural Science Foundation of China (21788102, 21490570, and 21490574), the Research Grant Council of Hong Kong (16305618, 16304819, N-HKUST609/19, C6009-17G, 16102918, T21-604/19-R, C6009-17G), the Science and Technology Plan of Shenzhen (JCYJ20160229205601482, JCYJ20170818113602462, JCYJ20180306180231853, and JCYJ 20180306174910791), the Innovation and Technology Commission (ITC-CNERC14SC01), and the Natural Science Foundation of Guangdong Province (2019B121205002 and 2019B030301003).

REFERENCES

- (1) Forrest, S. R.; Thompson, M. E. *Chem. Rev.* **2007**, *107*, 923.
- (2) Ostroverkhova, O. *Chem. Rev.* **2016**, *116*, 13279.
- (3) Moliton, A.; Hiorns, R. C. *Polym. Int.* **2004**, *53*, 1397.
- (4) Li, Q. Q.; Li, Z. *Acc. Chem. Res.* **2020**, *53*, 962.
- (5) Kuwabara, J.; Kanbara, T. *Macromol. Rapid Commun.* **2020**, 2000493.
- (6) Leclerc, M.; Morin, J. F. *Design and synthesis of conjugated polymers*. John Wiley & Sons: **2010**.
- (7) Liu, X. L.; Han, T.; Lam, J. W. Y.; Tang, B. Z. *J. Macromolecular Rapid Communications* **2020**, 2000386.
- (8) Takeda, Y.; Data, P.; Minakata, S. *Chem. Commun.* **2020**, 56, 8884.
- (9) Bura, T.; Blaskovits, J. T.; Leclerc, M. *J. Am. Chem. Soc.* **2016**, *138*, 10056.
- (10) Wencel Delord, J.; Glorius, F. *Nat. Chem.* **2013**, *5*, 369.
- (11) Qin, A. J.; Tang, L.; Lam, J. W. Y.; Jim, C. K. W.; Yu, Y.; Zhao, H.; Sun, J. Z.; Tang, B. Z. *Adv. Funct. Mater.* **2009**, *19*, 1891.
- (12) Barbujani, G.; Magagni, A.; Minch, E.; Cavalli Sforza, L. L. *PNAS* **1997**, *94*, 4516.
- (13) Ng, P. C.; Henikoff, S. *Nucleic Acids Res.* **2003**, *31*, 3812.
- (14) Zhu, C. Y.; Yang, B.; Zhao, Y.; Fu, C. K.; Tao, L.; Wei, Y. *Polym. Chem.* **2013**, *4*, 5395.
- (15) Lee, I. H.; Kim, H.; Choi, T. L. *J. Am. Chem. Soc.* **2013**, *135*, 3760.
- (16) Kreye, O.; Tóth, T.; Meier, M. A. *J. Am. Chem. Soc.* **2011**, *133*, 1790.
- (17) Kakuchi, R. *Angew. Chem. Int. Ed.* **2014**, *53*, 46.
- (18) Hu, R. R.; Li, W. Z.; Tang, B. Z. *Macromol. Chem. Phys.* **2016**, *217*, 213.
- (19) Dömling, A. *Chem. Rev.* **2006**, *106*, 17.
- (20) Kimyonok, A.; Wang, X. Y.; Weck, M. *J. Macromol. Sci. Polymer. Rev.* **2006**, *46*, 47.
- (21) Marella, A.; Tanwar, O. P.; Saha, R.; Ali, M. R.; Srivastava, S.; Akhter, M.; Shaquiquzzaman, M.; Alam, M. M. *Saudi. Pharm. J.* **2013**, *21*, 1.

- (22) Bangcuyo, C. G.; Rampey Vaughn, M. E.; Quan, L. T.; Angel, S. M.; Smith, M. D.; Bunz, U. H. *Macromolecules* **2002**, *35*, 1563.
- (23) Stille, J. K. *Macromolecules* **1981**, *14*, 870.
- (24) Umerani, M. J.; Dibble, D. J.; Wardrip, A. G.; Mazaheripour, A.; Vargas, E.; Ziller, J. W.; Gorodetsky, A. A. *J. Mater. Chem. C* **2016**, *4*, 4060.
- (25) Dibble, D. J.; Umerani, M. J.; Mazaheripour, A.; Park, Y. S.; Ziller, J. W.; Gorodetsky, A. A. *Macromolecules* **2015**, *48*, 557.
- (26) Fu, W. Q.; Dong, L. C.; Shi, J. B.; Tong, B.; Cai, Z. X.; Zhi, J. H.; Dong, Y. P. *Macromolecules* **2018**, *51*, 3254.
- (27) Peshkov, V. A.; Pereshivko, O. P.; Van der Eycken, E. V. *Chem. Soc. Rev.* **2012**, *41*, 3790.
- (28) Chan, C. Y. K.; Tseng, N. W.; Lam, J. W. Y.; Liu, J. Z.; Kwok, R. T. K.; Tang, B. Z. *Macromolecules* **2013**, *46*, 3246.
- (29) Liu, Y. J.; Gao, M.; Lam, J. W. Y.; Hu, R. R.; Tang, B. Z. *Macromolecules* **2014**, *47*, 4908.
- (30) Wei, B.; Li, W. Z.; Zhao, Z. J.; Qin, A. J.; Hu, R. R.; Tang, B. Z. *J. Am. Chem. Soc.* **2017**, *139*, 5075.
- (31) Hu, Y. B.; Han, T.; Yan, N.; Liu, J. K.; Liu, X. L.; Wang, W. X.; Lam, J. W. Y.; Tang, B. Z. *Adv. Funct. Mater.* **2019**, *29*, 1902240.
- (32) Bharate, J. B.; Wani, A.; Sharma, S.; Reja, S. I.; Kumar, M.; Vishwakarma, R. A.; Kumar, A.; Bharate, S. B. *Org. Biomol. Chem.* **2014**, *12*, 6267.
- (33) Chen, R.; Gao, X. Y.; Cheng, X.; Qin, A. J.; Sun, J. Z.; Tang, B. Z. *Polym. Chem.* **2017**, *8*, 6277.
- (34) Hu, Y. B.; Lam, J. W. Y.; Tang, B. Z. *Chin. J. Polym. Sci.* **2019**, *37*, 289.
- (35) Zhang, H. K.; Zhao, Z.; McGonigal, P. R.; Ye, R. Q.; Liu, S. J.; Lam, J. W. Y.; Kwok, R. T. K.; Yuan, W. Z.; Xie, J. P.; Rogach, A. L. *Mater. Today* **2020**, *32*, 275.
- (36) Muthamma, K.; Sunil, D.; Shetty, P. *Mater. Today Chem.* **2020**, *18*, 100361.
- (37) Xu, Y. Y.; Zhang, F.; Feng, X. L. *Small* **2011**, *7*, 1338.
- (38) Han, T.; Gui, C.; Lam, J. W. Y.; Jiang, M. J.; Xie, N.; Kwok, R. T. K.; Tang, B. Z. *Macromolecules* **2017**, *50*, 5807.
- (39) Chen, X. H.; He, Z. H.; Kausar, F.; Chen, G.; Zhang, Y. M.; Yuan, W. Z. *Macromolecules* **2018**, *51*, 9035.

Table of Contents

